





Cite this: *Nanoscale*, 2020, **12**, 22674

Plasmon-induced electron injection into the large negative potential conduction band of Ga₂O₃ for coupling with water oxidation†

Yaguang Wang,^a Xu Shi,^a Tomoya Oshikiri,^a Shuai Zu,^a Kosei Ueno^b and Hiroaki Misawa^{a,c}  

In this study, an interfacial modification layer was applied to improve the plasmon-induced light energy conversion of a gallium(III) oxide (Ga₂O₃) photoelectrode, which possesses a much more negative conduction band potential compared with the reduction potential of photons to hydrogen. The plasmon-induced photocurrent generation under visible light irradiation was observed with Au nanoparticle-loaded Ga₂O₃ (Au-NPs/Ga₂O₃). An interfacial modification was carried out by depositing a titanium dioxide (TiO₂) thin-film layer on Au-NPs/Ga₂O₃ via atomic layer deposition. Since the surface states of TiO₂ possess excellent hole-trapping ability, this interfacial modification remarkably improved the generation of plasmon-induced photocurrent in the visible region. The photoelectric conversion efficiency of interfacially modified Au-NPs/Ga₂O₃ showed a TiO₂ thin-film thickness dependence because the migration of hot carriers was suppressed with increasing TiO₂ thickness. The Au-NPs/Ga₂O₃ photoelectrode modified with 2 nm-thick TiO₂ showed the best photoelectric conversion performance, and the thermodynamic energy conversion efficiency under irradiation with 600 nm light was approximately two times larger than that of the Au-NPs/TiO₂-thin film due to the extremely negative onset potential of Au-NPs/Ga₂O₃ with TiO₂. Therefore, the plasmonic Ga₂O₃ photoanode with the interfacial TiO₂ modification could provide both a high reduction ability for H₂ evolution and an oxidation ability for water oxidation, because of the negative conduction band of Ga₂O₃ and the hole-trapping property from TiO₂, respectively.

Received 1st September 2020,

Accepted 4th November 2020

DOI: 10.1039/d0nr06319c

rsc.li/nanoscale

Introduction

Solar water splitting to produce H₂ is a main topic in artificial photosynthesis. To achieve efficient overall water splitting, one indispensable condition is that the bottom of the conduction band (CB) of the semiconductor should be more negative than the reduction potential of H⁺/H (0 V vs. RHE).^{1,2} Therefore, gallium(III) oxide (Ga₂O₃), which possesses a negative CB (−1.0 to −1.5 V vs. RHE), is a promising photocatalyst for overall water splitting.^{3–6} The largely negative CB potential of Ga₂O₃ can also be applied to the reduction of carbon dioxide to CO or HCOOH.⁷ However, it is only able to utilize the ultraviolet

light of solar radiation due to its wide band gap (~4.9 eV).⁸ Band engineering is a standard method for extending the absorption edge of a material. Kudo *et al.* reported that doping In₂O₃ into β-Ga₂O₃ to form a solid solution could efficiently shift the absorption edge towards longer wavelengths, thus maintaining H₂ and O₂ evolution.⁹ Although the absorption edge can be shifted to longer wavelengths by the doping method, the visible light energy is still insufficiently utilized. Moreover, doping causes a positive shift in the CB, thereby decreasing the reduction potential of Ga₂O₃. Although other methods, such as the addition of cocatalysts and promoters, have also been applied to increase the catalytic performance of Ga₂O₃, the results are not ideal for the use of visible light.^{10–12}

Recently, localized surface plasmon resonance (LSPR) of noble metal nanoparticles (Au, Ag) has been increasingly studied because it can efficiently increase visible-light absorption and significantly enhance the electromagnetic near-field.^{13–15} Under LSPR excitation, hot carriers are generated in the metal nanoparticles.¹⁶ When settling metal nanoparticles on a semiconductor, a Schottky barrier forms at the interface, and hot carriers with energy higher than the Schottky barrier can transfer to the CB of the semiconductor, thus achieving

^aResearch Institute for Electronic Science, Hokkaido University, Sapporo, Japan.
E-mail: misawa@es.hokudai.ac.jp

^bDepartment of Chemistry, Faculty of Science, Hokkaido University, Sapporo, Japan

^cCenter for Emergent Functional Matter Science, National Chiao Tung University, Hsinchu, Taiwan

†Electronic supplementary information (ESI) available: Description of fabrication schematic. Morphology of Au-NPs. Near-field spectrum of different size of Au-NPs. *I*–*V*, *I*–*t* and Mott–Schottky curves. Schematic of charge transfer. See DOI: 10.1039/d0nr06319c



charge separation at the interface.^{17,18} The electrons transferred to the CB of the semiconductor take part in the reduction reactions, such as H₂ evolution, while the holes will be captured at the surface states of the semiconductor and participate in the oxidation reactions.¹⁹ Importantly, it is expected that this plasmon-induced electron transfer mechanism will not cause a positive shift in the CB of gallium oxide and that visible light will be used effectively while maintaining a high reduction ability.

In plasmon-induced artificial photosynthesis systems using n-type semiconductors, the reducing ability can be improved by changing the type of semiconductor; however, the important point is that it is necessary to efficiently induce water oxidation as the rate-determining step. First, to stably oxidize water for a long time, it is necessary to use an oxide semiconductor in which the photoanode itself is not further oxidized. Second, the surface condition of the photoanode that can efficiently capture holes is required. Recently, we successfully demonstrated that plasmon-induced water oxidation is highly sensitive to the surface states of the crystal facets of SrTiO₃, and Au nanoparticle-loaded SrTiO₃ that is terminated with a TiO₂ layer shows a high oxidation ability.²⁰ In addition, Murakoshi *et al.* also reported that TiO₂ was beneficial for water oxidation by studying the intermediate species during plasmon-induced oxygen evolution.²¹ Therefore, improving the hole-trapping ability at the interface by the surface states of TiO₂ is an efficient way to enhance the water oxidation efficiency.

In this study, plasmonic Au-NPs were decorated on the surface of single-crystal Ga₂O₃ (Au-NPs/Ga₂O₃) to utilize visible light without shifting its negative CB energy level, which is beneficial for reduction reactions, such as H₂ evolution. To improve the water oxidation reaction of the Au-NPs/Ga₂O₃ photoelectrode, we also proposed an interfacial modification using a thin TiO₂ layer with a nanometre-scale thickness that was deposited on Au-NPs/Ga₂O₃ by the atomic layer deposition (ALD) technique. Photocatalytic reactivities were evaluated by monitoring the photocurrent of the photoelectrochemical (PEC) reaction. Based on the excellent hole-trapping ability of the as-prepared material, the plasmon-induced holes are efficiently trapped in the surface states at the interfacial boundary between the Au-NPs and TiO₂ layer, which improves the water oxidation reactivity of the Au-NPs/Ga₂O₃ photoelectrode.

Results and discussion

To optimize the conditions for the plasmonic PEC reaction enhancement of Au-NP-loaded Ga₂O₃, we first investigated the particle size effect of Au-NPs loaded on Ga₂O₃ because the LSPR properties of Au-NPs were very sensitive to their size.^{22,23} Au-NPs with mean sizes ranging from 10 to 50 nm were fabricated on Ga₂O₃ by annealing Au films with various thicknesses, as depicted in Fig. S1.† Fig. 1a shows the extinction spectra of Au-NPs with different sizes loaded on Ga₂O₃. The LSPR peaks showed an obvious red-shift and a broadening of

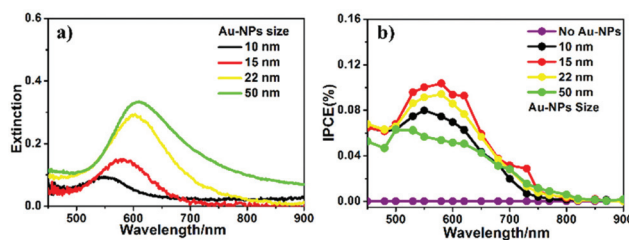


Fig. 1 (a) Extinction and (b) IPCE spectra of differently sized Au-NPs loaded on Ga₂O₃.

the full width at half maximum (FWHM) as the particle size increased. To evaluate the photocurrent conversion efficiency, we carried out incident photon-to-current efficiency (IPCE) measurements on all Au-NP/Ga₂O₃ photoelectrodes, as shown in Fig. 1b. Clear peaks were observed at approximately 580 nm in the IPCE action spectra of all Au-NPs/Ga₂O₃ photoelectrodes, and no detectable photo-response was obtained on the Ga₂O₃ photoelectrode without Au-NPs (see purple plot in Fig. 1b) in the visible wavelength region. In the case of Au-NP/Ga₂O₃ photoelectrodes loaded with small particles (≤ 15 nm), the IPCE band closely corresponded with the extinction spectrum of Au-NPs, indicating that the photocurrent was generated by the LSPR of Au-NPs.¹³ The 15 nm Au-NP-loaded Ga₂O₃ sample showed the best PEC performance with a peak IPCE value of 0.11% at 580 nm, as shown by the red curve in Fig. 1b. For the 10 nm Au-NP-loaded Ga₂O₃ sample, its low extinction value caused a lower IPCE than the 15 nm Au-NPs. In contrast, when the particle size became larger than 15 nm, the IPCEs decreased. A possible explanation for the observed decrease in IPCE was the LSPR decay mechanism. For large particles, instead of nonradiative decay, radiative decay becomes the main pathway for LSPR decay, which is unfavourable for electron-hole generation.^{24,25} The near-field enhancement spectra obtained by FDTD calculations (Fig. S2†) show a clear tendency that the large Au-NPs loaded on the Ga₂O₃ sample exhibited broadening of the LSPR peak, which was consistent with the extinction spectra. This broadening indicated a short dephasing time of LSPR due to significant radiation damping. Conclusively, Au-NPs/Ga₂O₃ with a particle size of 15 nm was the optimized photoelectrode for PEC photocurrent generation at visible wavelengths, and it was used in the following investigation.

To further improve the water oxidation ability of Au-NPs/Ga₂O₃, an interfacial modification was conducted by the introduction of a thin TiO₂ layer, which has a high hole-trapping ability. Because the CB alignment of TiO₂ is much more positive than that of Ga₂O₃, electrons cannot efficiently transfer from the CB of TiO₂ to that of Ga₂O₃.³ Therefore, a thin TiO₂ layer was deposited on Au-NPs/Ga₂O₃ as the final layer, as shown in Fig. S3,† to maintain direct contact between the Au-NPs and Ga₂O₃ and to provide effective charge separation. Moreover, Au-NPs were partially inlaid in the TiO₂ layer (inset in Fig. 2b) without destroying the direct contact between the Au-NPs and Ga₂O₃ by the reported ALD procedure of TiO₂.¹⁹



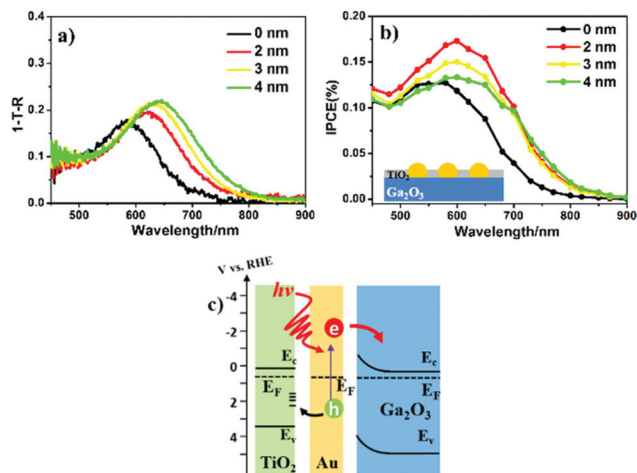


Fig. 2 (a) Absorption spectra and (b) IPCE action spectra of Au-NPs/ Ga_2O_3 modified with different thicknesses of TiO_2 . Inset: Cross-sectional schematic of $\text{TiO}_2/\text{Au-NPs}/\text{Ga}_2\text{O}_3$. (c) Schematic energy diagram showing the charge transfer in $\text{TiO}_2/\text{Au-NPs}/\text{Ga}_2\text{O}_3$.

With this structure, the plasmon-induced electrons could transfer from Au-NPs to Ga_2O_3 at the interface of Au-NPs/ Ga_2O_3 , and the hot holes could be captured at the surface states of TiO_2 , which might accelerate the water oxidation reaction. As a control experiment, TiO_2 was deposited between the Au-NPs and Ga_2O_3 . However, this arrangement was unfavourable for plasmon-induced charge separation, as discussed in detail in Fig. S6.†

The photoanodes of Au-NPs/ Ga_2O_3 with various thicknesses of the TiO_2 modification layer ($x\text{-nm-TiO}_2/\text{Au-NPs}/\text{Ga}_2\text{O}_3$, where $x = 2\text{--}4$) were investigated in the following section. The thickness of TiO_2 was precisely controlled by controlling the number of ALD cycles from 40 to 80. According to the XRD measurements in Fig. S4a,† all peaks measured from 10° to 70° show almost the same diffraction angle and width, indicating the same crystallinity of Ga_2O_3 before and after TiO_2 deposition. The bandgap (4.8 eV) of Ga_2O_3 estimated from the Tauc plots in Fig. S4b† kept the same before and after the deposition of TiO_2 . We also checked the elements oxidation states by XPS as shown in Fig. S5.† Ti 2p signal was presented after the deposition of TiO_2 . The new signal of Ti 2p provided the direct evidence of the TiO_2 deposition on Ga_2O_3 .²⁶ The binding energy of O 1s peak showed slightly broadening at the lower energy side rather than peak energy shift, which is ascribed to the presence of O 1s peak of Ti–O (529.8 eV) after TiO_2 deposition.²⁷ Additionally, the binding energy and the width of Ga 2p did not change after TiO_2 deposition. Based on the results above, it could be concluded that the crystallinity and band structure of Ga_2O_3 did not change after the deposition of TiO_2 . According to the top-view SEM in Fig. S7,† after the deposition of TiO_2 , the comparison of the morphology and particle size ($d_{\text{mean}} \sim 15$ nm) of Au-NPs before and after the deposition of the TiO_2 modification layer indicated that the ALD process at 300°C barely affected the morphology of Au-NPs on Ga_2O_3 .

Light absorption and carrier separation are two main factors contributing to photocurrent generation. To directly study the relationship between light absorption and PEC properties, the absorption spectrum of Au-NPs was calculated as the difference between the $(1 - T - R)$ spectrum of substrate with Au-NPs and without Au-NPs in Fig. 2a, where T and R are the transmission and reflection, respectively. Since the particle size and distribution of Au-NPs were similar, the red-shift of the peak position of the LSPR band from 585 to 645 nm was mainly caused by the refractive index increase in the surrounding media after TiO_2 deposition.²⁵ In addition, the absorption value at the LSPR peak also increased as the thickness of the TiO_2 layer increased. In contrast, the absorption at wavelengths shorter than 550 nm maintained almost the same value, which was only determined by the interband transition of Au.¹⁹ The PEC performance of these modified samples is presented in Fig. 2b, and all the $\text{TiO}_2/\text{Au-NPs}/\text{Ga}_2\text{O}_3$ photoelectrodes show an IPCE increase in the visible region compared with that of the Au-NPs/ Ga_2O_3 photoelectrode. Notably, 2-nm- $\text{TiO}_2/\text{Au-NPs}/\text{Ga}_2\text{O}_3$ showed the maximum IPCE value, which reached 0.17% at approximately 600 nm. Moreover, the stable photocurrent under 600 nm irradiation was approximately 1.5 times larger than that of Au-NPs/ Ga_2O_3 , as shown in Fig. S8.† The photocurrent of 2-nm- $\text{TiO}_2/\text{Au-NPs}/\text{Ga}_2\text{O}_3$ also showed a good stability because the photocurrent after 7.5 hours irradiation maintained 90% of the initial value of quasi-steady photocurrent, as shown in Fig. S9.† This result indicated that the interfacial modification by TiO_2 was beneficial for improving the PEC performance of Au-NPs/ Ga_2O_3 . Notably, after comparing the 2-nm- $\text{TiO}_2/\text{Au-NPs}/\text{Ga}_2\text{O}_3$ and pristine Au-NPs/ Ga_2O_3 , the IPCE peak of 2-nm- $\text{TiO}_2/\text{Au-NPs}/\text{Ga}_2\text{O}_3$ increased by 1.5 times, while the absorption increased by only 1.1 times at the peak LSPR wavelength. We suspect that much better charge separation occurred at the interface, resulting from the good hole-capturing ability of TiO_2 , which was an important factor for IPCE enhancement, as depicted in Fig. 2c. After the deposition of TiO_2 , the surface states of TiO_2 efficiently capture the plasmon-induced holes for efficient water oxidation. Moreover, the hot electrons generated at the Au-NPs/ Ga_2O_3 interface could be smoothly transferred to the CB of Ga_2O_3 due to the direct contact between Au and Ga_2O_3 . Based on this mechanism, hot carriers should have enough energy to achieve the hot-electron injection and water oxidation. The flat-band potential of 2-nm- $\text{TiO}_2/\text{Au-NPs}/\text{Ga}_2\text{O}_3$ was estimated to be -0.80 V vs. RHE after the deposition of 2 nm TiO_2 as shown in Fig. S10a.† The energy barrier between the flat-band potential of Ga_2O_3 for hot-electron injection and the oxidation potential of water ($+1.23$ V vs. RHE) is estimated as 2.03 eV (610 nm). Therefore, under the irradiation of light with the wavelength of 600 nm which is the peak wavelength of the IPCE action spectrum in Fig. 2b, both hot-electron injection and water oxidation can be achieved simultaneously.

As shown in Fig. 2a and b, the redshift of the $\text{TiO}_2/\text{Au-NPs}/\text{Ga}_2\text{O}_3$ IPCE peaks is not as obvious as their redshift in the absorption spectra. This observation could be explained by the threshold of photon energy needed for exciting electron/hole



separation at the Au-NPs/Ga₂O₃ interface, as discussed in Fig. S10.† This result suggested another insight, in that the electron injected into the CB of Ga₂O₃ had a high negative potential energy. The energy generated under light irradiation at 600 nm on the Ga₂O₃ photoanode, η_{photo} , was evaluated by being compared to an ideally nonpolarizable dark electrode as expressed in formula (1)

$$\eta_{\text{photo}} = \frac{I_{\text{max}}(1.23 \text{ V vs. RHE} - V_{\text{max}})}{P_{\text{in}}} \times 100(\%) \quad (1)$$

where I_{max} and V_{max} are the maximum output current and voltage, which generate the maximum electric power, respectively. P_{in} is the incident light intensity.²⁸

The value of η_{photo} is the thermodynamic energy-conversion efficiency of the photoelectrode, and the η_{photo} value for 2-nm-TiO₂/Au-NPs/Ga₂O₃ under light irradiation at 600 nm was calculated as 0.06% from the I - V characteristics shown in Fig. S11.† This value was approximately twice as large as that of the Au-NPs/TiO₂-thin film (0.03%) due to the extremely negative onset potential. Therefore, the plasmonic Ga₂O₃ photoanode modified with the thin TiO₂ layer could simultaneously achieve water oxidation and hot-electron injection with a negative reduction potential under visible light irradiation.

To further verify the hole-trapping ability of the TiO₂ layer, the IPCE values of 2-nm-TiO₂/Au-NPs/Ga₂O₃ and Au-NPs/Ga₂O₃ were measured in an electrolyte with triethanolamine (TEOA), as shown in Fig. 3. TEOA is a sacrificial hole scavenger due to its fast reaction kinetics based on one-electron oxidation.²⁹ For Au-NPs/Ga₂O₃ without TiO₂ modification, the oxidation reaction with water by holes was difficult, as discussed above. The addition of TEOA dramatically increased the oxidation reactivity even though the hole-trapping ability of the Ga₂O₃ surface was poor, as illustrated in Fig. S12a.† The high IPCE of 2-nm-TiO₂/Au-NPs/Ga₂O₃ without TEOA in Fig. 3b indicated that the hot holes trapped at the surface states of 2-nm-TiO₂/Au-NPs/Ga₂O₃ oxidized water efficiently even without the addition of TEOA, as shown in Fig. S12b.† Although the hole-trapping ability of TiO₂ could improve the oxidation reactivity and charge separation, the positive effect of interfacial modification on the IPCE showed a dependence on the thickness of TiO₂. When the TiO₂ thickness was larger than 2 nm, the IPCE improvement decreased even though the

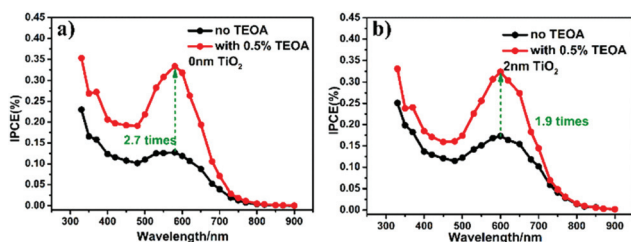


Fig. 3 IPCE action spectra of (a) Au-NPs/Ga₂O₃ and (b) 2-nm-TiO₂/Au-NPs/Ga₂O₃ measured in a KClO₄ aqueous solution with and without TEOA.

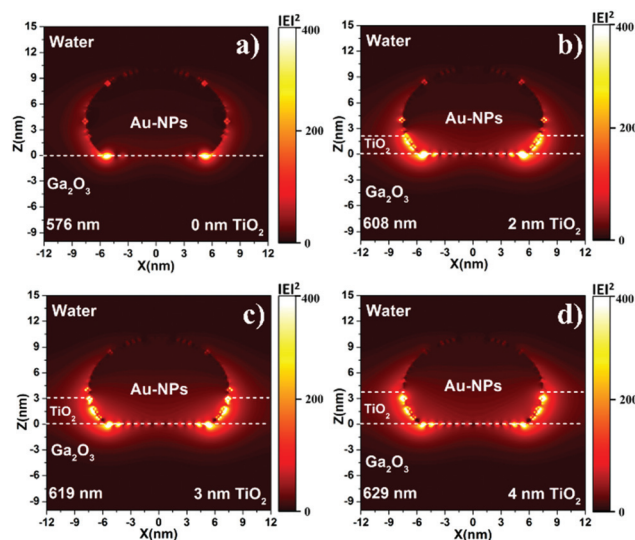


Fig. 4 Near-field distributions of Au-NPs/Ga₂O₃ modified with (a) 0, (b) 2, (c) 3, and (d) 4 nm TiO₂ layers, which was calculated by an FDTD simulation.

absorption increased. To understand the PEC performance difference of TiO₂/Au-NPs/Ga₂O₃ with different thicknesses of the TiO₂ layer, the near-field distribution at the interface of TiO₂/Au-NPs/Ga₂O₃ that determined the plasmon-induced carrier generation was calculated by a finite-difference time-domain (FDTD) simulation (Fig. 4). For Au-NPs/Ga₂O₃, the hot spot of the near-field was located at the interface between Au-NPs and Ga₂O₃, which are represented as the two bright spots in Fig. 4a. Regarding 2-nm-TiO₂/Au-NPs/Ga₂O₃, the near-field intensity was enhanced at the three-phase boundary of TiO₂/Au-NPs/Ga₂O₃ (Fig. 4b). However, the near-field intensity at the three-phase boundary decreased as the TiO₂ thickness increased (Fig. 4c and d). Though the near-field became stronger at the interface of TiO₂/Au-NPs with increasing distance from the Ga₂O₃ surface in Fig. 4c and d, the carriers generated at the Au-NPs/TiO₂ interface and then injected into the CB of TiO₂ contributed less to the IPCE, as discussed in Fig. S6.† Moreover, trapped holes at the three-phase boundary should migrate to the surface to participate in the water oxidation reaction. The thick TiO₂ modification layer would also suppress hole migration to the surface because of the extended path. Consequently, 2-nm TiO₂ interfacial-modified Au-NPs/Ga₂O₃ showed the best PEC improvement.

Conclusions

We demonstrated plasmon-induced photocurrent generation on wide bandgap Ga₂O₃ under visible light irradiation. The IPCE of Au-NPs/Ga₂O₃ was improved by an interfacial modification consisting of the deposition of a TiO₂ layer, which exhibits a high hole-trapping ability. The partial inlaying of Au-NPs with the TiO₂ layer could be beneficial for trapping plasmon-induced holes at the interfacial boundary between Au-NPs and



TiO₂ and improving the oxidation reactivity while maintaining efficient electron transfer. The 2-nm-thick TiO₂ interfacial modification shows up to a 1.5-times higher IPCE in the visible region than that without TiO₂. The thermodynamic energy-conversion efficiency for the 2-nm-TiO₂/Au-NPs/Ga₂O₃ photoelectrode under light irradiation at 600 nm was approximately twice as large as that of the Au-NPs/TiO₂-thin film due to the extremely negative onset potential.

Based on the above observations, the plasmonic Ga₂O₃ photoanode with the interfacial modification of a thin TiO₂ layer could demonstrate both a high ability for reduction, such as H₂ evolution, and oxidation ability for water oxidation because of the negative CB of Ga₂O₃ and the hole-trapping property of TiO₂, respectively. We believe this interfacial modification has enormous potential for use in artificial photosynthesis and could be applied in various fields and devices for photon energy conversion through structural optimization.

Materials and methods

Sample fabrication and structure characterization

The Sn-doped single-crystal β -Ga₂O₃ wafer (Novel Crystal Technology, Inc.) with an orientation of (−201) was cut to a size of 9.0 × 9.0 × 0.7 mm³. These Ga₂O₃ substrates were successively rinsed with acetone and methanol in an ultrasonic bath for 5 min each. To fabricate Au-NPs on the surface of Ga₂O₃, a thin gold layer was deposited onto the substrates by electron-beam evaporation at room temperature. The deposition pressure was approximately 2.0 × 10^{−6} Pa, and the evaporation rate was set to approximately 0.16 Å s^{−1}. Subsequently, the samples were annealed in air at 800 °C for 1 h. The fabrication processes are shown in Fig. S3 in the ESI.† The particle size of Au-NPs was controlled by changing the thickness of the Au film. The TiO₂ layer was deposited by a commercial hot-wall flow-type ALD reactor (SUNALETM R series, Picosun, Finland) at 300 °C with a deposition rate of 0.05 nm per cycle. TiCl₄ and deionized water vapor were used as the Ti and O sources, and N₂ was used as the carrier gas and purge gas. The pulse time and purge time were set as 0.1 and 4.0 s, respectively. X-Ray diffraction chart was applied to check the phase structure of Ga₂O₃ by RIGAKU RINT-2000/PC using Cu K α radiation. The valence of Ga, Ti and O was measured by an X-ray photoelectron spectrometer (XPS, JPS-9200, JEOL).

Optical properties and morphology characterization

A photonic multichannel analyser (PMA C7473, Hamamatsu Photonics) system was applied to measure the optical reflectance and transmittance spectra. Bandgap of Ga₂O₃ was estimated by the Tauc plots obtained from the transmittance spectra measured by A UV-Vis spectrophotometer (UV-3100PC, SHIMADZU). The surface morphology was identified by field-emission scanning electron microscopy (FE-SEM, JSM-6700FT, JEOL) with a maximum resolution of 1 nm. Additionally, ImageJ software was used to analyse the mean particle size.

Photoelectrochemical measurement

To obtain the ohmic contact, an In–Ga alloy with a weight ratio of 4 : 1 was coated on the backside and sidewall of the Au-NPs/Ga₂O₃ substrates. Then, the samples were connected to a copper plate in a Teflon reaction cell, which was connected to an electrochemical analyser (ALS/CH Instruments 852C, ALS) with a copper lead wire. The irradiation window consisted of a pinhole with a diameter of 2.0 mm on the lid of the cell. A three-electrode system consisting of a platinum wire and a saturated calomel electrode (SCE) as the counter electrode and reference electrode, respectively, was applied to measure the PEC properties. In addition, a 0.1 M KClO₄ aqueous solution without an electron donor was used as the electrolyte. During the photocurrent measurement, a potential of +0.3 V vs. SCE was applied to the working photoelectrode. The IPCE was calculated by formula (2):

$$\text{IPCE}(\lambda) = \frac{1240 \times I(\text{A cm}^{-2})}{\lambda(\text{nm}) \times P_{\text{in}}(\text{W cm}^{-2})} \quad (2)$$

where I is the photocurrent density, λ is the wavelength of incident light and P_{in} is the incident light intensity. In addition, Mott–Schottky experiments were carried out at a constant frequency of 5000 Hz in a scan window of −1.5 to 1.0 V vs. SCE in the three-electrode system described above.

Numerical simulations

Full-field electromagnetic wave simulations were performed using the FDTD method (FDTD Solutions, Lumerical). The investigated structure was simulated using perfectly matched layers along the z-direction and periodic boundary conditions along the x- and y-directions with a period of 20 nm. An ellipsoid sphere with a diameter of 15 nm in the x and y directions and 10 nm in the z direction was used to model the Au-NPs. In the simulation, the refractive index of Au was taken from the optical constants of Johnson and Christy. Ga₂O₃ and TiO₂ were treated as dielectric materials with refractive indices of 1.8 and 2.4, respectively.

Conflicts of interest

There are no conflicts to declare.

Acknowledgements

We acknowledge financial support from JSPS KAKENHI (Grant No. JP18H05205, JP18K05053, JP19H02737, JP19H04667, JP20H05083, and JP20K15113), the Nanotechnology Platform (Hokkaido University), and the Dynamic Alliance for Open Innovation Bridging Human, Environment and Materials (Five-Star Alliance) of MEXT.

Notes and references

- 1 L. Ni, M. Tanabe and H. Irie, *Chem. Commun.*, 2013, **49**, 10094–10096.



- 2 K. Maeda and K. Domen, *J. Phys. Chem. C*, 2007, **111**, 7851–7861.
- 3 M. Navarrete, S. Cipagauta-Díaz and R. Gómez, *J. Chem. Technol. Biotechnol.*, 2019, **94**, 3457–3465.
- 4 Y. Sakata, Y. Matsuda, T. Nakagawa, R. Yasunaga, H. Imamura and K. Teramura, *ChemSusChem*, 2011, **4**, 181–184.
- 5 Y. Sakata, T. Nakagawa, Y. Nagamatsu, Y. Matsuda, R. Yasunaga, E. Nakao and H. Imamura, *J. Catal.*, 2014, **310**, 45–50.
- 6 Y. Hou, X. Wang, L. Wu, Z. Ding and X. Fu, *Environ. Sci. Technol.*, 2006, **40**, 5799–5803.
- 7 H. Tsuneoka, K. Teramura, T. Shishido and T. Tanaka, *J. Phys. Chem. C*, 2010, **114**, 8892–8898.
- 8 T. Oshima, K. Kaminaga, H. Mashiko, A. Mukai, K. Sasaki, T. Masui, A. Kuramata, S. Yamakoshi and A. Ohtomo, *Jpn. J. Appl. Phys.*, 2013, 52.
- 9 A. Kudo and I. Mikami, *J. Chem. Soc., Faraday Trans.*, 1998, **94**, 2929–2932.
- 10 H. Kong, H. Li, G. Lin and H. Zhang, *Catal. Lett.*, 2011, **141**, 886–894.
- 11 Y. Sakata, Y. Matsuda, T. Yanagida, K. Hirata, H. Imamura and K. Teramura, *Catal. Lett.*, 2008, **125**, 22–26.
- 12 T. Yanagida, Y. Sakata and H. Imamura, *Chem. Lett.*, 2004, **33**, 726–727.
- 13 X. Shi, K. Ueno, T. Oshikiri and H. Misawa, *J. Phys. Chem. C*, 2013, **117**, 24733–24739.
- 14 Z. Zheng, W. Xie, B. Huang and Y. Dai, *Chem. – Eur. J.*, 2018, **24**, 18322–18333.
- 15 A. Abdalla, I. Khan, M. Sohail and A. Qurashi, *Sol. Energy*, 2019, **181**, 333–338.
- 16 X. Ma, Y. Dai, L. Yu and B. Huang, *Light: Sci. Appl.*, 2016, **5**, e16017.
- 17 K. Wu, J. Chen, J. McBride and T. Lian, *Science*, 2015, **349**, 632–635.
- 18 C. Clavero, *Nat. Photonics*, 2014, **8**, 95–103.
- 19 X. Shi, K. Ueno, T. Oshikiri, Q. Sun, K. Sasaki and H. Misawa, *Nat. Nanotechnol.*, 2018, **13**, 953–958.
- 20 X. Shi, X. Li, T. Toda, T. Oshikiri, K. Ueno, K. Suzuki, K. Murakoshi and H. Misawa, *ACS Appl. Energy Mater.*, 2020, **3**, 5675–5683.
- 21 K. Suzuki, X. Li, Y. Wang, F. Nagasawa and K. Murakoshi, *ACS Energy Lett.*, 2020, **5**, 1252–1259.
- 22 S. Bera, J. Lee, S. Rawal and W. Lee, *Appl. Catal., B*, 2016, **199**, 55–63.
- 23 P. Reineck, D. Brick, P. Mulvaney and U. Bach, *J. Phys. Chem. Lett.*, 2016, **7**, 4137–4141.
- 24 R. Sundararaman, P. Narang, A. Jermyn, W. Goddard and H. Atwater, *Nat. Commun.*, 2014, **5**, 5788.
- 25 C. Sonnichsen, T. Franzl, T. Wilk, G. von Plessen, J. Feldmann, O. Wilson and P. Mulvaney, *Phys. Rev. Lett.*, 2002, **88**, 077402.
- 26 M. Warwick, G. Carraro, E. Toniato, A. Gasparotto and C. Maccato, *Surf. Sci. Spectra*, 2016, **23**, 61–69.
- 27 B. Bharti, S. Kumar, H. Lee and R. Kumar, *Sci. Rep.*, 2016, **6**, 323.
- 28 R. Coridan, A. Nielander, S. Francis, M. McDowell, V. Dix, S. Chatman and N. Lewis, *Energy Environ. Sci.*, 2015, **8**, 2886–2901.
- 29 Y. Pellegrin and F. Odobel, *C. R. Chim.*, 2017, **20**, 283–295.

